Earth and Planetary Science Letters 445 (2016) 125–135

Contents lists available at ScienceDirect

Earth and Planetary Science Letters

www.elsevier.com/locate/epsl

The fluid budget of a continental plate boundary fault: Quantification from the Alpine Fault, New Zealand

Catriona D. Menzies [a,*], Damon A.H. Teagle [a,*], Samuel Niedermann [b], Simon C. Cox [c], Dave Craw [d], Martin Zimmer [b], Matthew J. Cooper [a], Jörg Erzinger [b]

[a] Ocean and Earth Science, National Oceanography Centre Southampton, University of Southampton, SO14 3ZH, UK
[b] Helmholtz Centre Potsdam, GFZ German Research Centre for Geosciences, Telegrafenberg, 14473 Potsdam, Germany
[c] GNS Science, Private Bag 1930, Dunedin 9054, New Zealand
[d] Department of Geology, University of Otago, Dunedin 9016, New Zealand

ARTICLE INFO

Article history:
Received 6 October 2015
Received in revised form 24 March 2016
Accepted 29 March 2016
Available online 19 April 2016
Editor: M. Bickle

Keywords:
Alpine Fault
fluid flux
mantle CO_2
helium isotopes
meteoric water
fault seal

ABSTRACT

Fluids play a key role in modifying the chemical and physical properties of fault zones, which may prime them for repeated rupture by the generation of high pore fluid pressures and precipitation of commonly weak, secondary minerals. Fluid flow paths, sources and fluxes, and the permeability evolution of fault zones throughout their seismic cycles remain poorly constrained, despite their importance to understanding fault zone behaviour. Here we use geochemical tracers of fluid–rock exchange to determine budgets for meteoric, metamorphic and mantle fluids on a major compressional tectonic plate boundary. The Alpine Fault marks the transpressional Pacific–Australian plate boundary through South Island, New Zealand and appears to fail in regular (329 ± 68 yrs) large earthquakes ($M_w \sim 8$) with the most recent event in 1717 AD. Significant convergent motion has formed the Southern Alps and elevated geothermal gradients in the hangingwall, which drive crustal fluid flow. Along the Alpine Fault the Alpine Schist of the Pacific Plate is thrust over radiogenic metasedimentary rocks on the Australian plate. The absence of highly radiogenic ($^{87}Sr/^{86}Sr > 0.7200$) strontium isotope ratios of hangingwall hot springs and hydrothermal minerals formed at a range of depths in the Alpine Fault damage zone indicates that the fluid flow is restricted to the hangingwall by a cross-fault fluid flow barrier throughout the seismogenic crust. Helium isotope ratios measured in hot springs near to the Alpine Fault (0.15–0.81 R_A) indicate the fault is a crustal-scale feature that acts as a conduit for fluids from the mantle. Rock-exchanged oxygen, but meteoric water-like hydrogen isotope signatures of hydrothermal veins indicate that partially rock-exchanged meteoric fluids dominate down to the top of the brittle to ductile transition zone at ~6 km. Geochemical tracer transport modelling suggests only ~0.02 to 0.05% of total rainfall west of the Main Divide penetrates to depth, yet this recharge flux is sufficient to overwhelm other fluid contributions. Calculated mantle fluid fluxes of CO_2 and H_2O (0.2 and 3 to 13 mol/m^2/yr respectively) and metamorphic H_2O fluxes (4 to 750 mol/m^2/yr) are considerably lower than the focused meteoric water discharge flux up the Alpine Fault (4×10^3 to 7×10^4 mol/m^2/yr), driven by the >3000 m hydrologic head of the Southern Alps. Meteoric waters are primarily responsible for modifying fault zone permeability during fluid–rock interactions and may facilitate the generation of high pore fluid pressures that could assist episodic earthquake rupture.

1. Introduction

Despite the importance of fluids in the evolution of faults throughout their seismic cycles by controlling heat and chemical transport (Blanpied et al., 1992) and influencing fault failure mechanics (Sibson, 1992), there are few observations that quantify the fluid origins, fluxes, and flow paths on active fault zones. Conceptual models suggest that fault zone permeability is dynamic, evolving from highly permeable, directly post rupture, to effectively sealed by the deposition of secondary minerals in pore spaces due to earthquake-related pulses of fluid (Byerlee, 1993) and compaction of fault gouge (Blanpied et al., 1992; Sleep and Blanpied, 1992). Fluids may facilitate earthquake nucleation when elevated pore fluid pressures reduce the effective normal stress, and previous studies have predicted that large faults require high pore

* Corresponding authors.
E-mail addresses: c.menzies@soton.ac.uk (C.D. Menzies), Damon.Teagle@Southampton.ac.uk (D.A.H. Teagle).

http://dx.doi.org/10.1016/j.epsl.2016.03.046

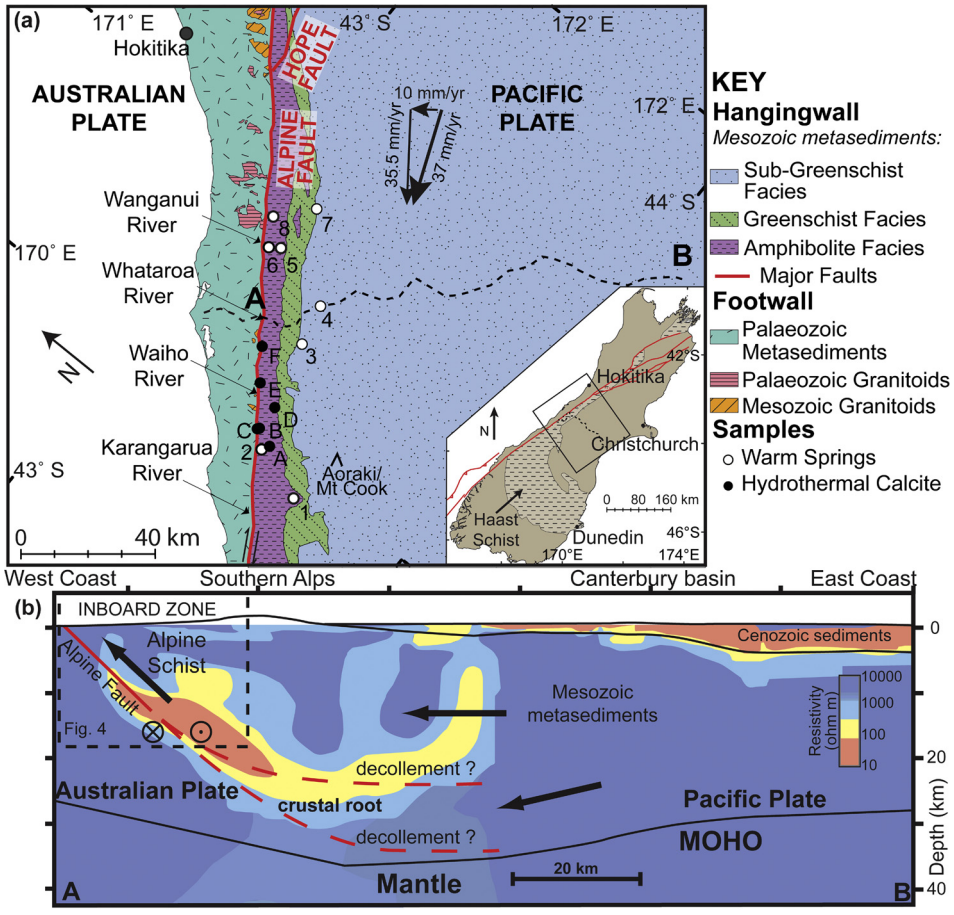

Fig. 1. (a) Geological map of South Island, New Zealand. Sample locations are outlined in the Supplementary data files Tables S3 and S4. Dashed line indicates resistivity cross-section AB. (b) Crustal-scale cross section incorporates fault model of Van Avendonk et al. (2004) and resistivity model from Jiracek et al. (2007). Dashed box signifies the area presented as Fig. 4.

fluid pressures to explain fault zone weakness and episodic earthquake rupture (Blanpied et al., 1992; Rice, 1992). Using assumed hydrological conditions, modelling has provided estimates of fluid fluxes and flow rates required to maintain overpressure in near-vertical strike slip faults (e.g. Faulkner and Rutter, 2001), and identified possible fluid sources; mantle fluids (Fulton and Saffer, 2009; Kennedy et al., 1997; Rice, 1992); metamorphic fluids (Fulton et al., 2009); meteoric fluids (Blanpied et al., 1992; Byerlee, 1993; O'Neil, 1984). However, the relative contributions of different fluid sources have not been constrained by direct observations for a plate boundary fault zone. Here we apply geochemical tracers of fluid–rock interaction to the unique geometry of the Alpine Fault, New Zealand, to develop the first fully integrated fluid budget and to quantify fluid sources, fluxes, and flow paths of a major continental fault zone.

1.1. Geological setting

The Alpine Fault is the transpressional Pacific–Australian plate boundary through the South Island, New Zealand that accommodates the majority of the relative strike slip motion (~23–25 mm/yr, Norris and Cooper, 2007). To accommodate ~10 mm/yr plate convergence, the Alpine Fault dips at ~45° to the south east and has dip-slip rates of 10 mm/yr, locally up to >12 mm/yr (Norris and Cooper, 2007). This geometry has formed the >3000 m high Southern Alps. Because the Alpine Fault has uplifted its ~1 km wide damage zone, surface outcrops and shallow boreholes provide a unique profile of deformation and fluid flow through a complete crustal section (Fig. 1) (Norris and Cooper, 2007). The low elevation Australian Plate footwall is composed of Palaeozoic metasediments and minor (<5%) Palaeozoic to Mesozoic granitoids (Cox and Sutherland, 2007). These rocks are juxtaposed by the Alpine Fault against hangingwall Pacific Plate quartzofeldspathic late Paleozoic to early Mesozoic metasediments, with minor metabasalt, metamorphosed into amphibolite-facies Alpine Schist.

The Alpine Fault fails in regular large earthquakes (~ M_w 7 to 8) (Sutherland et al., 2007) and is late in its 329 ± 68 yr seismic cycle, having last ruptured in 1717 AD (Berryman et al., 2012). Rapid uplift caused by ca. 10 mm/yr Alpine Fault dip slip (Norris and Cooper, 2007) and very high erosion rates in the Southern Alps have elevated geothermal gradients and the base of the brittle to ductile transition zone (BDTZ) in the hangingwall (Koons, 1987), resulting in a relatively thin seismogenic crust (8–10 km) (Boese et al., 2012). The high topography and geothermal gradient drive meteoric fluid flow (Menzies et al., 2014). This has resulted in warm springs hosted by the Alpine Schist up to 17 km east of the fault (Fig. 1a) and the deposition of quartz, chlorite, adularia, calcite, and gold-bearing veins from the near-surface down to the BDTZ (Menzies et al., 2014). Regions of low resistivity and seismic velocity imaged in the middle crust have been interpreted to be zones of metamorphic dehydration (Fig. 1b; Wannamaker et al., 2002).

At shallow levels the Alpine Fault has a <0.5 m-thick clay-rich principal slip zone and the related damage zone is predominantly developed in the hangingwall from the mylonitic Alpine Schist. This damage zone comprises 10 to ~60 m of strongly hydrothermally altered cataclasites and breccias with common fractures filled by calcite and clay minerals (Norris and Cooper, 2007; Schleicher et al., 2015; Toy et al., 2015; Warr and Cox, 2001). Shal-

low drilling across the Alpine Fault in the ~150 m deep DFDP-1b borehole measured a 0.53 MPa fluid overpressure from the hangingwall to the footwall, indicating the principal slip zone is impermeable to cross-fault fluid flow in the near-surface (Sutherland et al., 2012). This is in agreement with laboratory measurements of low permeability in Alpine Fault gouges (10^{-20} m^2) and cataclasites (10^{-15}–10^{-18} m^2) (Boulton et al., 2012; Carpenter et al., 2014).

2. Methods

2.1. Spring water sampling

Spring water samples for $\delta^{13}C_{DIC}$ determinations were collected in new 1 L or 60 mL, acid-cleaned HDPE bottles with minimal headspace, then sealed with parafilm tape. Samples for trace element analysis were filtered through 0.2 µm filter paper and acidified (with 1 mL/L quartz distilled concentrated HNO_3). Very heavy rainfall events can impact the local geothermal systems (Cox et al., 2015) and sampling during such events was avoided. Alkalinity was determined in the field by titration with 0.1 N HNO_3. Total alkalinity was calculated using the Gran Function Plot method.

For gas geochemistry analyses, spring waters were sampled in copper tubes sealed by steel clamps. These samples were not acidified or filtered because these processes promote degassing and therefore fractionation of the isotopes between dissolved and gaseous phases. In addition, at four locations free gas bubbling through water pools was sampled directly in glass flasks after filling them with spring water and replacing the water with gas. To identify if interaction with organic particulate material occurred after sampling we compare $\delta^{13}C$ values for degassed water samples and gas samples. All of these are slightly lower in the gas samples indicating that no interaction with organic material post sampling occurred in these samples (see Supplementary Materials Tables S1 and S2).

2.2. $^{87}Sr/^{86}Sr$ and Sr concentration measurements

Spring waters and hydrothermal calcite veins were prepared and measured using the Isotope Geochemistry class 100 clean laboratory suite at the University of Southampton.

Hydrothermal calcite dissolution

For each sample 10–20 mg of pure calcite was handpicked from a crushed mineral vein. The mineral separates were then sonicated in Milli-Q water (18.2 MΩ H_2O), dried and hand crushed using an agate mortar and pestle. ~10 mg of sample was then dissolved in 0.5 M analytical grade or ROMIL sub-boiled acetic acid.

Determination of strontium concentrations

Dissolved calcite samples and spring waters were analysed for strontium concentrations using a PerkinElmer Optima 4300 DV ICP-OES. Samples were appropriately diluted with 2% sub-boiled HNO_3, as were synthetic multi-element standards used to calibrate the instrument. Precision and accuracy were assessed using international reference solution SLRS4 and in-house reference material Sco2/15. Precision was better than 2.8%, accuracy better than 8%, and detection limits were 0.05 ppb for these measurements.

$^{87}Sr/^{86}Sr$ determination

Strontium was separated from dissolved whole rocks, calcite and spring waters using Sr-spec resin following Harris et al. (2015). Over the course of the study strontium isotopes were measured on two VG Sector 54 Thermal Ionisation Mass Spectrometers (TIMS) and a ThermoFisher Scientific TritonPlus TIMS. Precision and accuracy were assessed using international reference material NBS987. The average values for $^{87}Sr/^{86}Sr$ of NBS987 on the three instruments were 0.710241 ± 0.000027 (2σ, $n = 70$) and 0.710241 ± 0.000019 (2σ, $n = 71$) for the two VG Sector 54 instruments and 0.710244 ± 0.000019 (2σ, $n = 135$) for the Triton Plus. Internal precision was monitored by measuring 150 ratios for each sample and calculating 2 standard errors of these measurements (standard errors are reported in Tables S3 and S4). Strontium column blanks were <10 pg.

2.3. Gas geochemistry

At GFZ Potsdam, chemical compositions of free gas samples were determined using an Omnistar (Pfeiffer Vacuum) quadrupole mass spectrometer and then appropriate volume splits were analysed for noble gas concentrations and isotopic compositions following Niedermann et al. (1997). Measured $^3He/^4He$ ratios and ^4He concentrations were corrected for air contamination based on ^{20}Ne following the method of Giggenbach et al. (1993).

Analyses of the total gas composition were performed using an Omnistar quadrupole mass spectrometer with a closed ion source, a mass range of 1 to 100 amu and a heated and temperature-regulated gas inlet system. The gas was transferred into the mass spectrometer with a flow rate of 1–2 cm^3/min at $\sim 5 \times 10^{-6}$ mbar pressure and analysed for H_2, He, CH_4, O_2, N_2, Ar, and CO_2. Calibration of the mass spectrometer was performed with certificated test gases at the same pressure conditions. The relative standard deviation (2σ, $n = 10$) of air components was <10%.

2.4. $\delta^{13}C$ determinations

Calcite

Microscopically interrogated, hand-picked, clean calcite was crushed with an agate mortar and pestle to provide ~1 mg of calcite powder. Analysis was carried out on the Europa GEO 20–20 mass spectrometer with a CAPS preparation system at the University of Southampton. Standard external analytical precision based on replicated analysis of in-house standards calibrated to NBS-19 is better than 0.1‰.

Dissolved inorganic carbon

Carbon isotope values of spring waters and total dissolved inorganic carbon (TDIC) were determined at the National Isotope Centre, GNS Science, New Zealand between 2009 and 2012. Water samples were reacted with 85% phosphoric acid, the resulting CO_2 extracted and purified to run in duel inlet mode on a Europa GEO 20–20 mass spectrometer. A sodium bicarbonate standard solution was analysed to check the extraction procedure. Carbonate content was calculated from the measured CO_2 pressures in milligrams of carbonate per kilogram of water. The $\delta^{13}C$ values are reported with respect to VPDB. Reported errors combine the statistical errors from sample and standard determinations, combined in quadrature with a system error component based on the analysis of an ongoing series of measurements on an oxalic acid standard.

3. Results

3.1. Strontium isotopes – fluid flow paths

The Alpine Fault juxtaposes isotopically distinct rocks. The footwall metasediments and minor (<5%, see Fig. 1) intrusive granitoids have high $^{87}Sr/^{86}Sr$ ratios (Buller Terrane metasediments $^{87}Sr/^{86}Sr = 0.7239$–1.0018; Adams, 2004; Pickett and Wasserburg, 1989; Tulloch et al., 2009; Table 1, Table S6). In contrast, the hangingwall Alpine Schist yields a narrow range of relatively low $^{87}Sr/^{86}Sr$ ratios ($^{87}Sr/^{86}Sr = 0.7039$–0.7137, average $= 0.7091 \pm 0.0019(1\sigma)$, $n = 45$, including data from Adams et al., 2009; Adams and Graham, 1997; Horton et al., 2003) (Table 1, Table S6, Fig. 2). As the host rocks either side of the Alpine Fault have similar strontium concentrations, we would expect comparable strontium concentrations in fluids associated with these rock types,

Table 1
Summary of strontium isotope data of host rocks either side of the fault, hangingwall spring waters, and hydrothermal calcites from all depths. References: 1—Adams et al. (2009); 2—Adams and Graham (1997); 3—Horton et al. (2003); 4—Adams (2004); 5—Tulloch et al. (2009); 6—Pickett and Wasserburg (1989).

	$^{87}Sr/^{86}Sr$		n	Ref.
	Range	Average $\pm 1\sigma$		
Hangingwall Alpine Schist	0.70391–0.71366	0.7091 ± 0.0019	45	1, 2, 3, new data current study
Footwall Buller Terrane Metasediments	0.72394–1.00182	0.7834 ± 0.0578	135	4, 5, 6
Footwall Granitoids	0.70846–0.77742	0.7354 ± 0.0255	11	5, 6
Spring Waters	0.70843–0.71130	0.7094 ± 0.0010	13 analyses of 8 springs	New data, current study
AFZ Hydrothermal Calcite	0.70405–0.71136	0.7079 ± 0.0017	41	New data, current study

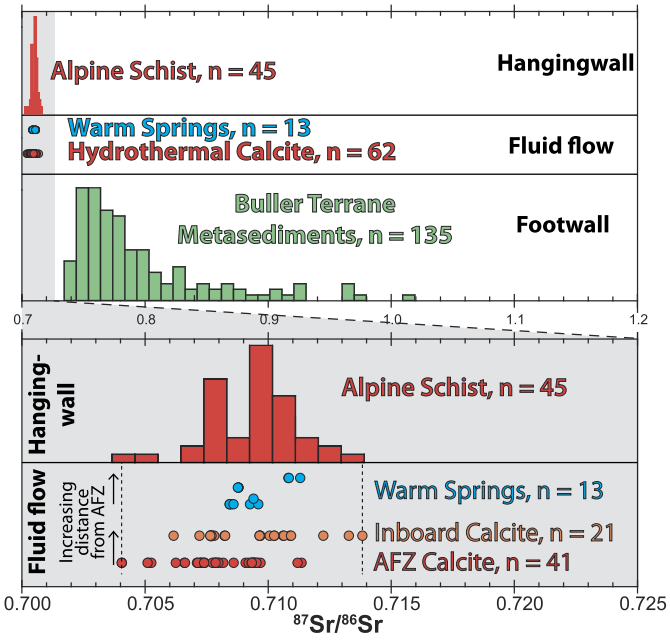

Fig. 2. The distributions of $^{87}Sr/^{86}Sr$ in footwall and hangingwall host rocks are compared with $^{87}Sr/^{86}Sr$ of hangingwall warm springs and hydrothermal minerals. Warm springs and hydrothermal minerals $^{87}Sr/^{86}Sr$ signatures are within range of hangingwall host rock Alpine Schist and do not appear to have obtained strontium from highly radiogenic footwall rocks. Footwall host rock data compiled from Adams (2004), Pickett and Wasserburg (1989), Tulloch et al. (2009) and hangingwall host rock data compiled from Adams et al. (2009), Adams and Graham (1997), Horton et al. (2003) along with new data collected in this study (see Table S6).

but $^{87}Sr/^{86}Sr$ ratios would be significantly more radiogenic in the footwall. We have measured $^{87}Sr/^{86}Sr$ of warm springs and hangingwall hydrothermal calcites to ascertain fluid flow paths. The $^{87}Sr/^{86}Sr$ ratios of spring waters (0.7084–0.7113, $n = 13$, Table S4), fault zone calcite veins formed throughout the fault zone from ductile to brittle conditions, and near-surface cataclasite and fault gouge cements (0.7041–0.7114, $n = 41$, Table S3) are all within range of hangingwall Alpine Schist host rocks (Fig. 2).

Fluid and vein mineral $^{87}Sr/^{86}Sr$ ratios subtly decrease with proximity to the Alpine Fault due an increased proportion (with proximity to the plate boundary) of metabasic rocks with lower $^{87}Sr/^{86}Sr$ ratios in the Alpine Schist mylonites (Cox and Sutherland, 2007). There is no evidence that fluids circulating and mineralising in the hangingwall have interacted with radiogenic Sr-bearing rocks of the footwall Australian Plate (Fig. 2). This indicates there has been no cross-fault fluid flow from the footwall to the hangingwall and suggests that hangingwall fluids are isolated from the footwall at depth. Further, the warm springs upwell above the Alpine Fault zone, not within it. There are no thermal springs in the footwall of our study area, and footwall cataclasites are less altered than those in the hangingwall (Toy et al., 2015). These observations together with low Alpine Schist-like strontium isotope ratios indicate that the Alpine Fault is a hydrologic barrier to cross-fault flow throughout the seismogenic crust.

3.2. Warm spring gas chemistry

Springs in the hangingwall of the Alpine Fault have discernible mantle He contributions, with $^3He/^4He$ >0.1 R_A (0.15–0.81 R_A, Fig. 3a, Tables S1, S2; R_A is the atmospheric $^3He/^4He$ ratio of 1.39×10^{-6}). Springs further from the fault have significantly lower $^3He/^4He$ signatures, indicative of crustal ^4He production (0.018–0.030 R_A) only, with no resolvable mantle contribution (Fig. 3a). These springs also have the highest ^4He concentrations (Fig. 3d), up to two orders of magnitude greater than those adjacent to the Alpine Fault. Given the uniformity of the host Alpine Schist this indicates that these spring waters have had longer transit times or flow paths and therefore have been subjected to a greater crustal production of ^4He by radioactive decay of uranium and thorium in the rock mass.

Warm springs contain abundant dissolved CO_2 (1–18 mmol/kg), and some springs effervesce CO_2 at the surface. Bicarbonate to calcium molar ratios of 7–19 in springs are considerably higher than can be accounted for through calcite dissolution (HCO_3^-/Ca^{2+} from 1–2), requiring an additional CO_2 source. Warm springs that have a contribution of mantle He have higher CO_2 concentrations than those with crustal $^3He/^4He$ signatures (4.1–18.4 mmol/kg, versus 1.0–3.0 mmol/kg, Fig. 3b, Table S1). These springs also have the highest carbon isotope ratios ($\delta^{13}C_{CO_2} = -11.6$ to -6.7‰ versus -16.8 to -12.3‰; Barnes et al., 1978; Fig. 3c, Tables S1 and S2). Most near-surface calcite cements in Alpine Fault cataclasites and gouges, and hydrothermal calcite veins yield calculated fluid $\delta^{13}C$ values within the crustal/ mantle range (-13.8 to -3.8‰, average -6.6 ± 1.7, $n = 59$, Table S5).

4. Discussion

4.1. Fluid budgets on the Alpine Fault

Although the Southern Alps are a major orogenic belt with rapid rates of uplift, there is no evidence for current magmatic activity in the Alpine Fault region. Consequently our potential fluid sources are limited to meteoric waters, fluids generated by metamorphic dehydration reactions, and mantle fluids. To estimate the fluxes of our different end member fluids up the Alpine Fault we use our geochemical measurements to quantify the relative contributions of these different fluid sources.

4.1.1. Calculating the mantle fluid flux

There is a mantle contribution of up to 10% He in geothermal waters near to the Alpine Fault, indicating the fault is a conduit for mantle-derived fluids into the upper crust, similar to other crustal-scale fault zones. A minimum upward flow rate of mantle He (q), which is the minimum rate at which a mantle fluid must move through the crust to overcome the crustal production of ^4He and retain the measured $^3He/^4He$ ratio, can be calculated following eq. (1) (Kennedy et al., 1997; Kulongoski et al., 2013):

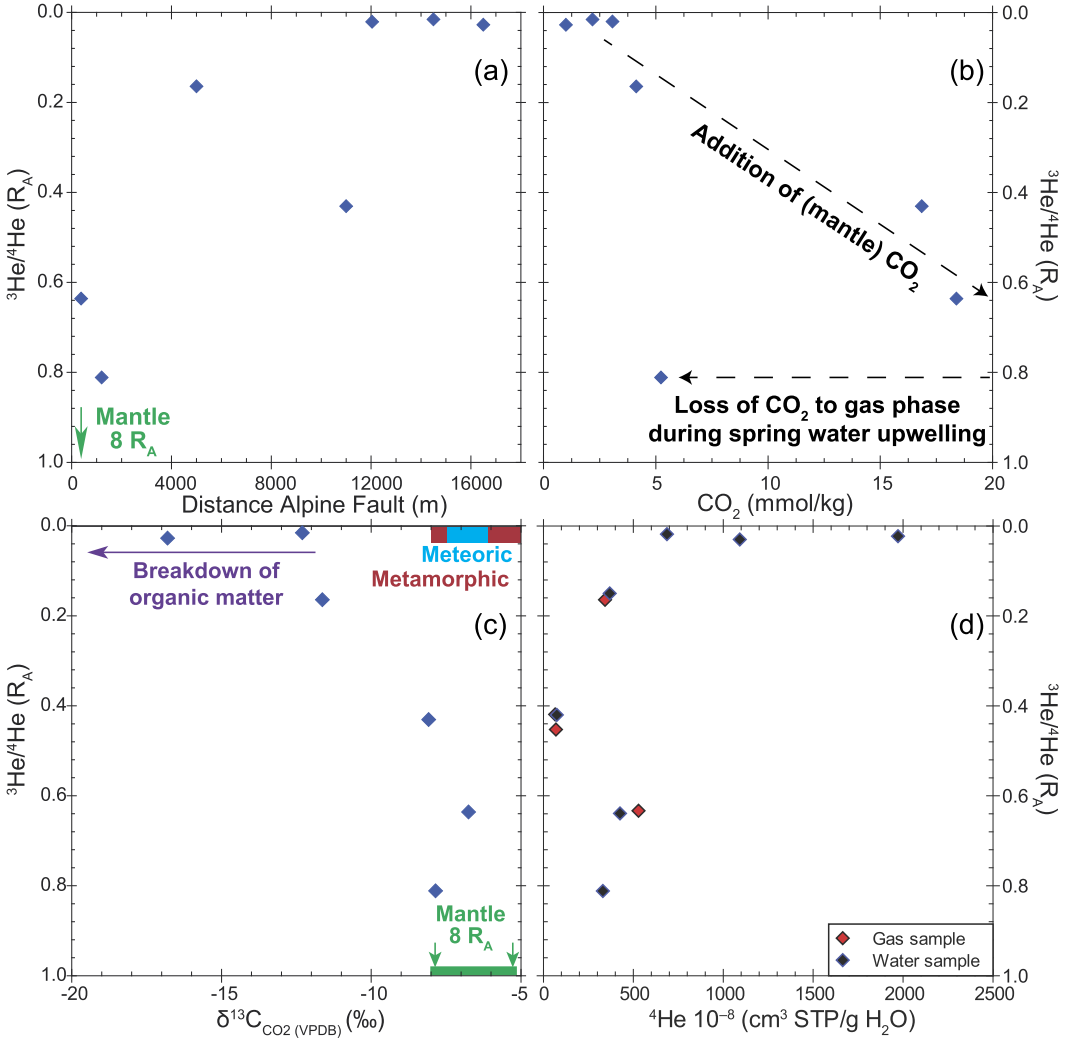

Fig. 3. (a) Air-corrected $^3He/^4He$ ratios versus distance southeast from the Alpine Fault. Springs closest to the Alpine Fault have a mantle helium contribution. (b) Air-corrected $^3He/^4He$ versus CO_2 concentrations in spring waters. Springs with elevated $^3He/^4He$ ratios distinctive of a mantle helium contribution have higher CO_2 concentrations than springs with only a crustal helium signature, indicating that the former have a contribution of mantle CO_2. Mantle $^3He/^4He$ value from Marty and Jambon (1987). (c) $\delta^{13}C$ values of warm spring waters that have a contribution of mantle He are higher than those with no mantle contribution. End member compositions from Jenkin et al. (1994) for carbon isotopes and Marty and Jambon (1987) for helium isotopes. (d) Total ^4He concentration versus $^3He/^4He$ ratio indicates that spring waters with no mantle contribution have the highest ^4He concentration and therefore the longest residence time.

$$q = \frac{h_{crust}\rho_r P_{(He)}}{\rho_f [^4He]_{f,m}} \times \left[\frac{R_s - R_c}{R_m - R_s}\right] \quad (1)$$

where h_{crust} is crustal thickness; ρ_f and ρ_r are fluid and solid densities respectively; $P_{(He)}$ is the ^4He solution rate ($cm^3STP/g\ H_2O/yr$), based on the production rate of ^4He, rock density, and the fractional effective porosity; $[^4He]_{f,m}$ is the original mantle fluid ^4He concentration; and R_c, R_m and R_s are the $^3He/^4He$ ratios in the crust, mantle and sample respectively. The key parameters determined in this study are: the calculated original mantle fluid ^4He concentrations ($[^4He]_{f,m}$), and the measured sample $^3He/^4He$ ratios (R_s) and ^4He concentrations ($[He_s]$, eq. (2)). Reasonable values for other parameters are estimated from published data: crustal thickness (h_{crust}), the crustal ^4He production rate ($P_{(He)}$) based on host rock concentrations of U and Th (see Table 2), $^3He/^4He$ ratios of crust (R_c) and mantle (R_m), and fluid and solid densities (ρ_f, ρ_r). Calculated mantle fluid flow rates for the Alpine Fault are between 0.42 and 2.6 m/yr. These rates are significantly higher than estimated for the San Andreas Fault (0.004–0.14 m/yr; Kennedy et al., 1997; Kulongoski et al., 2013), the North Anatolian Fault (~0.13 to 0.19 m/yr; de Leeuw et al., 2010) and the Karakoram Fault (~0.012–0.019 m/yr; Klemperer et al., 2013).

These minimum mantle flow rates can be converted into ^3He fluxes:

$$^3He\ flux = q \times \rho_f \times [He_s] \times R_s \quad \text{(Kulongoski et al., 2013)} \quad (2)$$

This yields ^3He fluxes of 2×10^{-11} to 9×10^{-11} $mol/m^2/yr$. These calculated mantle helium fluxes can be combined with a mantle fluid $CO_2/^3He$ ratio of 2×10^9 (Marty and Jambon, 1987) and a $H_2O/^3He$ ratio of 3×10^{10}–1×10^{11} (Hilton and Porcelli, 2003) to convert ^3He fluxes to CO_2 and H_2O fluxes. Using the spring with the highest $^3He/^4He$ ratio (Amythest spring), indicating least dilution by crustal ^4He, and these mantle $CO_2/^3He$ and $H_2O/^3He$ ratios, a CO_2 flux of 0.18 $mol/m^2/yr$ and a H_2O flux of 2.5 to 12.7 $mol/m^2/yr$ is calculated for a conduit up the Alpine Fault from the mantle (Table 2). Flow rates and fluxes calculated using other springs are outlined in the Supplementary Materials Tables S1 and S2, all springs that contain a mantle component have similar order of magnitude fluxes. These calculations rely on a number of parameters from published data, and those with the greatest influence on our results are the mantle $CO_2/^3He$ and $H_2O/^3He$ ratios, and the crustal production rate of ^4He. Changes in these values by 10% result in a 10% change in the fluxes calculated. The man-

Table 2
Calculation of the mantle fluid flux up the Alpine Fault following Kennedy et al. (1997), Kulongoski et al. (2013) and using measured values from Amythest Spring (see Table S4 for location details), which displays the highest $^3He/^4He$ ratio of all the springs measured in this study. Full calculations for each spring are outlined in Supplementary Materials Tables S1 and S2.

Calculation of the mantle fluid flux		
Measurements	*Amythest Spring*	
Sample $^3He/^4He$, R_s	0.81	R_A
Sample $^3He/^4He$, absolute ratio	1×10^{-6}	
^4He concentration of sample, ^4He_s	3×10^{-6}	cm^3 STP/g H_2O
^3He concentration of sample	4×10^{-12}	cm^3 STP/g H_2O
Mantle $^3He/^4He$ ratio, R_m	8	R_A
Mantle $^3He/^4He$ ratio, $^3He/^4He_m$, absolute ratio	1×10^{-5}	
Original ^4He mantle concentration, $^4He_{fm}$	3×10^{-7}	cm^3 STP/g H_2O
Crust $^3He/^4He$ ratio, R_c	0.02	R_A
U concentration in rock, U	3	ppm
Th concentration in rock, Th	13	ppm
Constants		
Porosity, $\varnothing$	0.1	kg/m/s
Crustal thickness, h_{crust}	35,000	m
Density rock, ρ_r	2700	kg/m^3
Density fluid, ρ_f	1000	kg/m^3
$CO_2/^3He$ ratio mantle	2×10^9	
$H_2O/^3He$ ratio mantle, min and max	3×10^{10}	1.4×10^{11}
^4He production rate, P ^4He		
$\rho_r \times (1.19 \times 10^{-13} \times U + 2.88 \times 10^{-14} \times Th) \times (1 - \varnothing)/\varnothing$	2×10^{-11}	$cm^3/g/yr$
^3He flow rate, q		
$(hc \times \rho_r \times PHe)/(\rho_f \times {}^4He_{fm}) \times (R_s - R_c)/(R_m - R_s)$	0.55	m/yr
^3He flux		
$q \times \rho_f \times {}^4He_s \times R_s$	2×10^{-10}	cm^3 STP/cm^2/yr
	9×10^{-11}	$mol/m^2/yr$
Mantle fluxes up the Alpine Fault		
Mantle H_2O flux maximum	12.6	$mol/m^2/yr$
Mantle H_2O flux minimum	2.5	$mol/m^2/yr$
Mantle CO_2 flux	0.18	$mol/m^2/yr$

tle $CO_2/^3He$ ratio used has been shown to be a robust estimate for the mantle component in gases in a range of geodynamic settings (Marty and Jambon, 1987). The mantle $H_2O/^3He$ ratio is more poorly constrained, and hence we use a range spanning an order of magnitude in our calculations. Crustal production rates are based on the U and Th concentrations measured in the host rocks. The ^4He solution rate is controlled by the fractional effective porosity of the system which is estimated as a maximum of 0.1 (for the uppermost crust where sampled spring waters circulate); if this value is halved, then the resulting flux estimates double owing to an increased ^4He solution rate.

Mantle fluids are reported in numerous fault-controlled, seismically active settings across New Zealand (Giggenbach et al., 1993). Seismicity in the mantle down dip of the Alpine Fault (Lamb et al., 2015), below the schematic lower-crustal décollement (Fig. 1b), may indicate the flow path for fluids from the mantle to the Alpine Fault conduit and up to the surface.

Boiling during the decompression path of these fluids may affect the $CO_2/^3He$ ratios and isotopic values, leading to decoupling of the isotopic tracers we use to investigate the mantle fluid flux. Boiling textures in the Inboard and Main Divide Zones of the Southern Alps indicate there has been immiscibility during the fluid flow history, as discussed in detail by Jenkin et al. (1994). Our primary data for the estimates of the mantle fluid flux are fluid and gas $^3He/^4He$ ratios. If these fluids have boiled, this generates fluids with lower $^3He/^4He$ ratios and gases with higher $^3He/^4He$ ratios as ^3He is preferentially lost to the gas phase. If this gas phase is redissolved in shallower level fluids the $^3He/^4He$ ratio of the resulting fluid would be higher, leading to larger estimates of the mantle fluid flux. However, when $CO_2/^3He$ and $^3He/^4He$ ratios are available for both fluid and gas for the same spring these are similar (see Supplementary Materials Tables S1 and S2). Also the variability in $^3He/^4He$ ratios of springs along strike adjacent to the Alpine Fault is minor (0.64–0.81 R_A; Supplementary Materials Tables S1 and S2) suggesting that although our estimates for mantle flow rates are maxima, we consider them to be close to the true value.

4.1.2. Calculating the metamorphic fluid flux

The rapid convergence of the Pacific and Australian plates in the Southern Alps region and the strong climate asymmetry caused by the orographic barrier of the Southern Alps leads to crustal thickening and the rapid movement of mid-crustal rocks through this orogen (Koons, 1990). The prograde metamorphism of greenschist facies Otago Schist to amphibolite facies Alpine Schist results in a change in the volatile content (ΔLOI) of ~1 wt.% (Pitcairn et al., 2014). This value can be combined with the thickness of rock undergoing dehydration (T) and the plate convergence rate (CR) to estimate a metamorphic fluid flux. In the crustal root of the Southern Alps a ~5 km thickness of rock is currently undergoing metamorphism to amphibolite facies (Pitcairn et al., 2014) and the plate convergence rate is ~0.01 m/yr (Norris and Cooper, 2007). We can calculate how much water is released from a 1 km strike length of the orogen in a year following:

$$Production\ of\ H_2O/year = \Delta LOI \times CR \times T \times L \times \rho_r \quad (3)$$

where L is the strike length and ρ_r is the rock density. Using reasonable values for rock density (Table 2), 8×10^7 mol/yr of H_2O per 1 km strike length would be liberated from the dehydrating root. The production rate is directly proportional to the thickness of the dehydrating root, the loss of volatiles during metamorphic dehydration reactions, and the convergence rate, all of

Table 3
Table outlining the different areas over which fluids may be focused from depth. Shown are calculated output fluxes over these areas for metamorphic and meteoric fluids compared with the mantle fluid flux up the Alpine Fault crustal conduit.

Fluid focusing areas	All on narrow AFZ	All on wider AFZ	Imaged Conductive Zone	Inboard Zone
Width (m)	100	1000	2000	20000
Strike length (m)	1000	1000	1000	1000
Area (m^2)	10^5	10^6	2×10^6	2×10^7
Total Metamorphic ($H_2O + CO_2$) Output Flux ($mol/m^2/yr$)	750	75	38	**4**
Metamorphic CO_2 Output Flux ($mol/m^2/yr$)	37.5	3.75	1.9	0.2
Meteoric H_2O Output Flux ($mol/m^2/yr$)	**2×10^4 to 4×10^4**	**2×10^3 to 4×10^3**	1.2×10^3	120
Mantle H_2O Flux ($mol/m^2/yr$)		**2.5 to 12.7**		
Mantle CO_2 Flux ($mol/m^2/yr$)		**0.2**		

which are well constrained in this system. Here we approximate the change in volatile content during metamorphism to amphibolite facies to be due to the loss of H_2O, although in reality CO_2 and other volatiles are also lost. Fluid inclusions in veins in the Inboard Southern Alps, but away from the Alpine Fault zone have ~5 mol.% CO_2 (Craw and Norris, 1993). Using this measurement the annual metamorphic CO_2 production is estimated to be $\sim 4 \times 10^6$ mol/yr per kilometre of orogen. Our calculations provide a long time scale estimate of metamorphic fluid production based on the plate convergence rates with a caveat that the instantaneous release rates may be episodically higher or lower than these estimates.

In order to compare this with our estimate of mantle fluid we must consider the area that this discharge flux is distributed over in three scenarios where all the metamorphic fluid is focused up: (1) a 100 m to 1000 m wide Alpine Fault zone; (2) the 2 km wide area imaged as a conductive zone in the SIGHT survey, interpreted as metamorphic waters at depth (Wannamaker et al., 2002; Fig. 1); and (3) assuming that upwelling metamorphic fluids are not focused but distributed over the entire area of the Inboard Zone from the Alpine Fault to the Main Divide of the Southern Alps (shown on Fig. 1b). The maximum metamorphic fluid flux estimate is 750 $mol/m^2/yr$ up a 100 m wide Alpine Fault zone and the minimum is 4 $mol/m^2/yr$ across the entire Inboard Zone of the Southern Alps (Table 3). 5% of this output flux is composed of metamorphic CO_2, and the minimum output CO_2 flux estimate is similar to the mantle CO_2 flux (Table 3). However, hydrogen isotope measurements of quartz and chlorite veins throughout the Alpine Fault zone yield strong meteoric water signatures with no requirement for a metamorphic fluid contribution to the mineralising fluids, and indicating that meteoric water fluid fluxes are orders of magnitude larger than the potential metamorphic fluid flux (Menzies et al., 2014).

4.1.3. Calculating the meteoric water fluid flux

The Southern Alps experience exceptionally high rainfall, locally exceeding 10 m/yr, but the infiltration rate of this rainfall deep into the mountains is poorly constrained. Infiltration rates of between 0.3 and 20% are estimated for shallow level penetration (10–100s of metres) of rainfall into the ridges of the Inboard Zone (Sims et al., 2015). Here we use relative tracer transport distances of O and H and the isotopic compositions of deeply formed quartz veins (6–8 km) to calculate likely proportions of rainfall that may reach mid-crustal levels and to estimate meteoric water fluid fluxes up the Alpine Fault.

Water circulating in the upper 2 km of the crust at temperatures <200 °C retains meteoric δD and δ^{18}O values (Menzies et al., 2014). Below 2 km, waters become partially equilibrated with rock and by the top of the BDTZ at ~6 km depth δ^{18}O values are equilibrated with the rocks, but δD values of deeply formed quartz veins still indicate formation from meteoric water (Menzies et al., 2014). These observations provide information on the relative tracer transport distances of the oxygen and deuterium meteoric water signature, which can be used to calculate the time-integrated fluid flux for this system (Bickle and McKenzie, 1987).

Firstly we estimate meteoric fluid fluxes using measured isotopic values of partially deformed vein minerals and fluid inclusions (Menzies et al., 2014). From mass balance, assuming the equilibrium fluid–rock tracer exchange for oxygen and hydrogen, the minimum transport distance (h) of a specific tracer is a function of the time integrated fluid flux ($\Sigma flux$) and the solid/fluid partition coefficient (K_d), following equation (4) (Bickle and McKenzie, 1987):

$$h = \Sigma flux/(\rho_s K_d/\rho_f) \quad (4)$$

The assumption of equilibrium fluid–rock tracer exchange is reasonable because fluid movement in the system of interest, below the active meteoric-dominated regime that feeds hot springs, is probably along grain boundaries, at elevated temperatures (>200 °C), and in fine-grained rocks, all factors that favour equilibrium isotopic exchange. Transport distances evaluated by isotopic measurements show that the fluid oxygen isotope values are rock dominated after a short flow distance (on the order of hundreds of metres) and fluid hydrogen isotope values remain meteoric-like at 6 km depth (4 km along the flow path). Using these distances we can estimate a time integrated fluid flux for this system. For tracer transport distances of ~120 and 4000 m, and ~300 and 10,000 m for oxygen and hydrogen respectively we estimate time integrated fluid fluxes between ~200 and ~500 m (m^3/m^2; equivalent to 1×10^7 to 2.6×10^7 mol/m^2) (Table 4). Note, that because groundwater strontium concentrations are low (0.1–21 mmol/L; Cox et al., 2015) fluids become rock-dominated at very small transport distances (2×10^{-3} to 1 m) for these time integrated fluid fluxes. As the hydrogen isotope values remain meteoric-like, with only minor rock influence, the transport distance must be greater than 4 km, implying that our estimated integrated fluid flux of 200 m is a minimum.

Secondly, we consider a column of rock of $4 \times 1 \times 1$ km^3 to estimate likely fluid fluxes as constrained by measured δ^{18}O and δD values of fluids in the middle crust. For reasonable values of crustal permeability between ~2 and 6 km depth ($k = 1 \times 10^{-15}$ to 1×10^{-17} m^2; Manning and Ingebritsen, 1999), fluid viscosity ($\mu = 2 \times 10^{-4}$ kg/m/s), fluid density at higher temperatures and pressures ($\rho_f = 0.9$ g/cm^3), and acceleration due to gravity ($g = 9.8$ m/s^2), we can estimate a hydraulic conductivity (K, m/s, Table 4) following:

$$K = (k \times \rho_f \times g)/\mu \quad (5)$$

Using hydraulic conductivity and the head gradient (height, y/length, x; 3000 m/20,000 m) of the orogen we can estimate the Darcy velocity (Q/A, Table 4) in $m^3/m^2/s$ following:

$$Q/A = K \times (y/x) \quad (6)$$

To calculate a fluid flux for the system we estimate the mass of water passing through the $4 \times 1 \times 1$ km^3 column following equation (7), over a reasonable time period (t) following:

Table 4
Meteoric water time integrated fluid flux calculations tested by tracer transport distances. Highlighted in bold are variables that estimate fluid fluxes that are within range of tracer transport distances shown in Menzies et al. (2014).

Meteoric water time integrated flux calculation							
Variables							
Permeability, k, m^2	1×10^{-15}	1×10^{-16}	**1×10^{-17}**	**1.5×10^{-17}**	**2.5×10^{-17}**	1×10^{-18}	
time, yrs	1000	10,000	100,000	100,000	100,000	100,000	
relief, y, m	3000	3000	3000	3000	3000	3000	
length, x, m	20,000	20,000	20,000	20,000	20,000	20,000	
Hydraulic conductivity, K, m/s							
$(k \times \rho_f \times g)/\mu$	4.5×10^{-8}	4.5×10^{-9}	4.5×10^{-10}	6.8×10^{-10}	1.1×10^{-9}	4.5×10^{-11}	m/s
Darcy velocity, Q/A, volume/area/s							
$K \times (y/x)$	6.8×10^{-9}	6.8×10^{-10}	6.8×10^{-11}	1×10^{-10}	1.7×10^{-10}	6.8×10^{-12}	m^3/m^2/s
	2.1×10^{-1}	2.1×10^{-2}	2.1×10^{-3}	3.2×10^{-3}	5.3×10^{-3}	2.1×10^{-4}	m^3/m^2/yr
Yearly input flux, volume/area/yr							
$Q/A \times \rho_f$	1.9×10^{2}	1.9×10^{1}	**1.9×10^{0}**	**2.9×10^{0}**	**4.8×10^{0}**	1.9×10^{-1}	kg/m^2/yr
	1.1×10^{4}	1.1×10^{3}	**1.1×10^{2}**	**1.6×10^{2}**	**2.7×10^{2}**	1.1×10^{1}	mol/m^2/yr
Time integrated flux, t, yrs							
$Q/A \times \rho_f \times t$	1.9×10^{5}	1.9×10^{5}	**1.9×10^{5}**	**2.9×10^{5}**	**4.8×10^{5}**	1.9×10^{4}	kg
	1.1×10^{7}	1.1×10^{7}	**1.1×10^{7}**	**1.6×10^{7}**	**2.7×10^{7}**	1.1×10^{6}	mol
Tracer transport distance, h							
O, $\Sigma flux/(\rho_s K_d/\rho_f)$ (<1 km)	*127*	*127*	***127***	***190***	***317***	*13*	m
H, $\Sigma flux/(\rho_s K_d/\rho_f)$ (>4 km)	*4177*	*4177*	***4177***	***6265***	***10442***	*418*	m

$$Mass\ H_2O = Q/A \times t \times \rho_f \quad (7)$$

To match the fluid fluxes calculated from tracer transport modelling above, permeabilities towards the lower end of those commonly estimated for the middle crust, or times shorter than 100,000 yrs are required. For hydrogen transport distances of 4000 to 10,000 m permeabilities of 1×10^{-17} m^2 to 2.5×10^{-17} m^2 and 100,000 yrs or 1×10^{-16} m^2 to 2.5×10^{-16} m^2 and 10,000 yrs are required to maintain the time-integrated fluid flux of $\sim 1.1 \times 10^7$ to 2.7×10^7 mol of water (Table 4). In agreement with our tracer transport calculations we prefer higher fluid flux estimates that give greater tracer transport distances. These may be obtained with a marginally higher minimum permeability (1.5×10^{-17} m^2 or 1.5×10^{-16} m^2 over 100,000 and 10,000 yrs respectively) which would give hydrogen tracer transport distances of ~6000 m and a revised minimum fluid flux of 160 mol/m^2/yr (100,000 yrs) or 1600 mol/m^2/yr (10,000 yrs) (Table 4). Measurements of mean fluid residence times are required to fully constrain fluid flow in these systems, but here we prefer the longer, more reasonable time of 100,000 yrs. Therefore tracer transport modelling indicates an input flux of meteoric waters to deeper crustal levels, under reasonable crustal permeability conditions is between ~160 and 250 mol/m^2/yr. This is equivalent to ~0.02 to 0.05% of rain falling at the surface being transported to ~6 km depth, between one and three orders of magnitude lower than estimates of near-surface infiltration rates (Sims et al., 2015).

Strongly altered Alpine Fault rocks with a high proportion of clay and carbonate minerals (Sutherland et al., 2012; Toy et al., 2015) indicate the Alpine Fault zone has experienced higher fluxes of water and CO_2 than the adjacent crust where there is little evidence for retrogression of the metamorphic amphibolite facies mineral assemblages. ^{3}He/^{4}He ratios indicate that the Alpine Fault is a conduit for mantle fluids throughout the crust and strontium isotope ratios preclude large scale fluid movement from footwall to the hangingwall. This combination of up-fault conduit and across-fault fluid-flow barrier indicates the development of a structure that focuses the flow of deeply infiltrating meteoric fluids driven by the topographic head of the >3000 m Southern Alps that channels upwelling meteoric fluids back towards the surface.

Using our estimated input fluxes, which are constrained using tracer transport distances estimated from isotopic measurements of fluids at depth, we can estimate fluxes on the Alpine Fault zone assuming focusing of fluid up different fault areas. Using the same scenarios as for the metamorphic fluid estimates (Table 3) these yield maximum fluid fluxes up a 100 m to 1000 m wide fault zone of 2×10^4 to 4×10^4 mol/m^2/yr and 2×10^3 to 4×10^3 mol/m^2/yr respectively, and a minimum fluid flux, assuming no focusing up the fault with outflow dispersed over the Inboard Zone, of 120 mol/m^2/yr. Due to the geometry of the orogen, where hydraulic gradients focus fluid flow away from the Main Divide towards the impermeable barrier of the Alpine Fault, and the strong alteration of Alpine Fault zone rocks, we consider the focused estimates most reasonable.

4.2. The balance between fluid sources in the Alpine Fault zone

Hydrogen isotopic data indicates that only meteoric waters are detectable down to middle crustal levels in the Southern Alps (Jenkin et al., 1994; Menzies et al., 2014). If the meteoric water infiltration flux is discharged on the Alpine Fault whereas metamorphic waters regionally leak out throughout the Inboard Zone (Table 3), the meteoric water flux is two to three orders of magnitude higher than the metamorphic flux. In contrast, if metamorphic and meteoric waters are focused over the same area, the meteoric water flux remains significantly higher than the metamorphic flux, by an order of magnitude. Studies of the San Andreas Fault suggest that it is difficult to focus metamorphic fluids derived by regional metamorphic processes into zones of high fluid pressure on a near vertical fault (Fulton et al., 2009). However, the Alpine Fault dips at ~45–50° and is projected to flatten at depth to intersect a conductive, seismic low velocity zone at ~20 km (Fig. 1b), considered to be a metamorphic fluid production zone (Wannamaker et al., 2002). Therefore it is possible that metamorphic-derived fluids may be channelled up the Alpine Fault. Alternatively they may regionally leak out over the Inboard Zone, evidenced by late stage vein mineralisation throughout the Alps. Either way, the meteoric water flux is at least one order of magnitude higher than the metamorphic flux. ^{3}He/^{4}He data indicates that mantle fluids move up the Alpine Fault from the mantle to the near-surface. However, if estimated mantle fluid fluxes are compared with our estimated meteoric water fluxes over any area, they are at least four times to an order of magnitude lower than meteoric waters (Table 2).

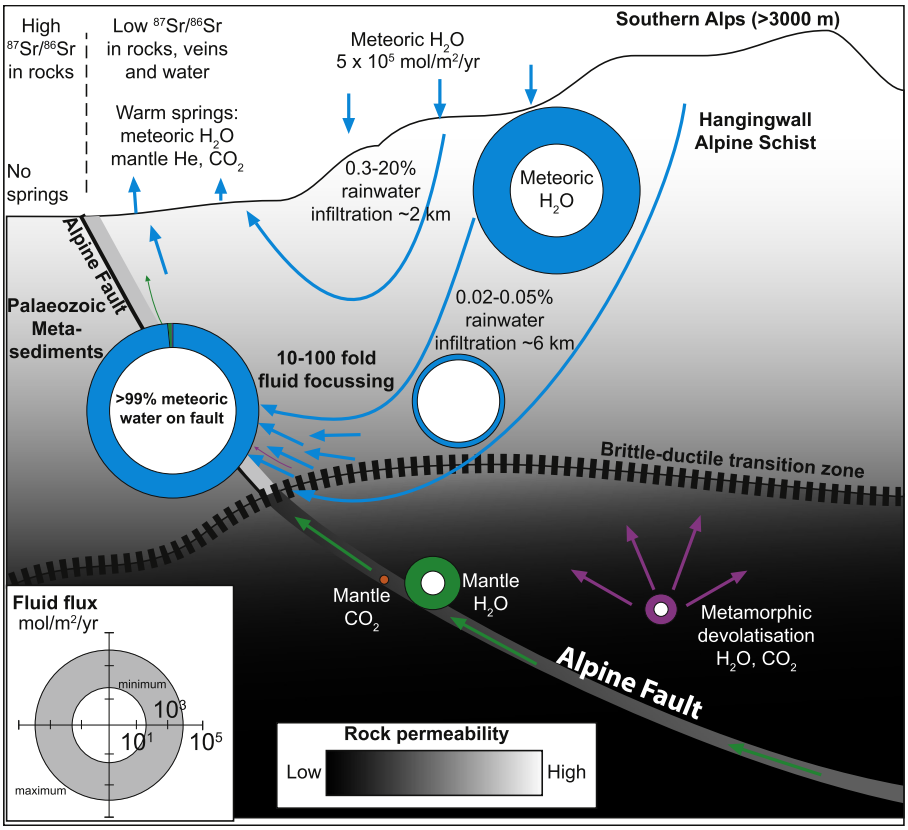

Fig. 4. Detailed view of the area of interest highlighted in Fig. 1b. Estimated fluxes of meteoric, metamorphic and mantle fluids are shown as coloured circles, with the inner and outer circles representing minimum and maximum estimates respectively. The proportion of each end member fluid that constitutes the flux up the Alpine Fault is illustrated as a proportional circle, meteoric water making up >99% of the total flux up the Alpine Fault. Initial rainwater infiltration ranges from Sims et al. (2015). Aspects of this figure are based on observations and data from quartz veins reported in Menzies et al. (2014).

4.3. Fluid focusing

Strontium isotope data indicates that fluid flow in the Southern Alps orogen is restricted to the hangingwall of the fault and a low permeability cross-fault fluid flow barrier exists in the plane of the fault throughout the seismogenic crust. The damage zone of the Alpine Fault consists of a low permeability principal slip zone (PSZ) surrounded by a highly fractured, partially sealed, more permeable zone 10 to ~60 m wide (Sutherland et al., 2012). In the hangingwall this damage zone is overprinted by an "alteration zone" where intense fluid–rock reactions have occurred, altering primary amphibolite facies minerals to clay minerals and carbonate (Sutherland et al., 2012; Toy et al., 2015). This zone of alteration, as well as mantle $^3He/^4He$ signatures in springs near to the Alpine Fault, provide evidence for the focusing of fluid flow through a small volume of rock in the hangingwall of the Alpine Fault zone that provides a conduit from the mantle to the near surface. Laboratory permeability measurements of fault rocks from the Nojima fault zone, Japan (Lockner et al., 2009) show that although the PSZ gouge has very low matrix permeability, the damage zone surrounding the PSZ has higher matrix permeability than the rocks outside the fault zone, and therefore has the capacity to channel fluids up the fault zone, whereas the low permeability PSZ gouge acts as a barrier to cross fault fluid flow (Lockner et al., 2009). This situation is comparable to the Alpine Fault zone, where a low permeability PSZ must extend throughout the seismogenic crust, as evidenced by strontium isotope ratios of vein minerals, and above this the hangingwall damage zone has been altered by fluids that have been channelled up the fault zone.

Taking this into consideration, we infer that the regional meteoric water recharge flux is concentrated onto a 100 to 1000 m wide fault discharge zone. We therefore present a meteoric fluid flux on the Alpine Fault of 2×10^3 to 4×10^4 mol/m^2/yr, accounting for >99% of the fluid flowing through the Alpine Fault zone, if the metamorphic fluid flux is predicted to leak out over the entire Inboard Zone of the Southern Alps (Fig. 4). Incursion of large volumes of meteoric fluid into continental scale fault zones has been recorded elsewhere by meteoric-like isotopic signatures of alteration minerals in the San Andreas fault zone (O'Neil, 1984) and indicates that deeply-sourced high pressure fluids from the mantle or dehydration reactions need not be required to elevate pore fluid pressures in fault zones (Sleep and Blanpied, 1992).

4.4. Implications

High pressure fluids in fault zones have commonly been invoked to explain apparent fault weakness in studies of continental-scale fault zones. We show that a large flux of meteoric water passes through a limited rock volume in the hangingwall damage zone of the Alpine Fault, above the low permeability PSZ fault "seal" that extends throughout the seismogenic crust to ~8 km depth. Models predict a fluid flux of 10^{-2}–10^{-1} $m^3/m^2/yr$ may be needed to maintain high pore fluid pressures at 15 km depth in near-vertical fault zones with low cross-fault permeability and at least three orders of magnitude permeability anisotropy (Faulkner and Rutter, 2001). Our estimates for the flux of water through the Alpine Fault zone are within this range (4×10^{-2}–8×10^{-1} $m^3/m^2/yr$), indicating enough water may flow through the Alpine Fault zone such that high pore fluid pressures could be generated which may contribute to fault weakening and episodic fault rupture.

In addition, the presence of these fluids may impact on fault weakening by promoting retrogression of primary minerals to

weaker phyllosilicate minerals through fluid–rock interactions in the damage zone of the fault. Fluid pressures in this region may be elevated when secondary minerals precipitate and infill fractures, isolating fluids in high pressure pockets within the damage zone (Blanpied et al., 1992; Byerlee, 1993), so-called pressure compartmentalisation (Fulton and Saffer, 2009) and creep compaction may lead to the development of pore fluid overpressures in the fault core (Sleep and Blanpied, 1992). These processes may weaken the fault by reducing the effective normal stress, facilitating slip at low shear stress (Rice, 1992).

Our strontium isotope data indicating fluid flow paths are restricted to the Alpine Fault's hangingwall suggests that the cross-fault fluid flow barrier measured in shallow boreholes extends throughout the seismogenic crust. If such a low permeability material extends throughout the seismogenic crust it may affect earthquake rupture nucleation processes by facilitating thermal pressurisation and dynamic weakening (Carpenter et al., 2014).

5. Summary

We present the first fully integrated fluid budget for a major continental fault, the Alpine Fault (Fig. 4), using geochemical constraints on fluid sources, fluxes and flow paths ($^3He/^4He$, δD, $\delta^{18}O$, $\delta^{13}C$, $^{87}Sr/^{86}Sr$). We show that:

1. The Alpine Fault is a crustal-scale fault zone and acts as conduit for fluids from the mantle to the near surface. Clay and carbonate alteration in the Alpine Fault damage zone indicates a large flux of water and CO_2 has travelled through this zone and mantle $^3He/^4He$ ratios in warm springs near to the fault indicate the Alpine Fault is a conduit for a small flux of mantle fluids through the crust.
2. Strontium isotope analyses of warm springs and hydrothermal vein minerals indicate fluid flow is restricted to the hangingwall of the Alpine Fault and the fault acts as a barrier to cross-fault fluid flow throughout the seismogenic crust to ~8 km depth.
3. We identify fluid sources and independently calculate fluid fluxes from these sources in the Alpine Fault zone using $^3He/^4He$ ratios in warm springs and previously published stable isotope analyses of hydrothermal vein minerals. We calculate mantle H_2O and CO_2 fluxes of 2.5 to 12.6 mol/m^2/yr (4.5×10^{-5} to 2.3×10^{-4} m^3 STP m^{-2}/yr) and 0.2 mol/m^2/yr (4×10^{-3} m^3 STP m^{-2}/yr) respectively; a metamorphic H_2O flux of ~4 mol/m^2/yr (~7×10^{-5} m^3 STP m^{-2}/yr) distributed over the Inboard Zone of the Southern Alps and a maximum of 750 mol/m^2/yr focused up a 100 m wide fault zone; and a meteoric H_2O flux of 2×10^3 to 4×10^3 mol/m^2/yr (4×10^{-2} to 8×10^{-2} m^3 STP/m^2/yr) up to 2×10^4 to 4×10^4 mol/m^2/yr (4×10^{-1} to 8×10^{-1} m^3 STP/m^2/yr) focused up a 100 to 1000 m wide fault zone. Meteoric water dominates and constitutes >99% of the fluid channelled up the Alpine Fault zone.
4. Geochemical tracer transport modelling suggests only ~0.02 to 0.05% of total rainfall west of the Main Divide penetrates to the top of the brittle to ductile transition zone at 6 km depth, yet this recharge flux is sufficient to overwhelm other fluid contributions.
5. Focused fluid flow through the Alpine Fault zone may promote fault weakening by facilitating the formation of weak secondary minerals and promoting the generation of high pore fluid pressures or pressure compartmentalisation.

Acknowledgements

Samples were collected under Dept. of Conservation Permit WC-22994-GEO. C.D.M. acknowledges Natural Environment Research Council (NERC) CASE PhD studentship award NE/G524160/1 (GNS Science CASE partner). D.A.H.T. acknowledges NERC grants NE/H012842/1 and NE/J024449/1, and a Royal Society Wolfson Foundation Research Merit Award (WM130051). S.C.C was funded under GNS Science's "Impacts of Global Plate Tectonics in and around New Zealand Programme" (PGST Contract CO5X0203). The gas sampling and analyses have been supported by the Deutsche Forschungsgemeinschaft under grant NI 512/5-1. We thank Enzio Schnabel, Birgit Plessen, Darryl Green and Mike Bolshaw for help with analyses and Rachael James for advice on spring sampling and analyses. We gratefully acknowledge comments from Carolyn Boulton and Brett Carpenter on an early version of this manuscript, editorial advice and comments from Mike Bickle, and reviews from two anonymous reviewers that improved this manuscript.

Appendix A. Supplementary material

Supplementary material related to this article can be found online at http://dx.doi.org/10.1016/j.epsl.2016.03.046.

References

Adams, C.J., 2004. Rb–Sr and strontium isotopic characteristics of the Greenland Group, Buller Terrane, New Zealand, and correlations at the East Gondwanaland margin. N.Z. J. Geol. Geophys. 47, 189–200.
Adams, C.J., Campbell, H.J., Griffin, W.L., 2009. Tracing the Caples Terrane through New Zealand using detrital zircon age patterns and radiogenic isotope signatures. N.Z. J. Geol. Geophys. 52, 223–245.
Adams, C.J., Graham, I.J., 1997. Age of metamorphism of Otago Schist in eastern Otago and determination of protoliths from initial strontium isotope characteristics. N.Z. J. Geol. Geophys. 40, 275–286.
Barnes, I., Downes, C.J., Hurlston, J.R., 1978. Warm Springs, South Island New Zealand and their potentials to yield Laumontite. Am. J. Sci. 278, 1412–1427.
Berryman, K.R., Cochran, U.A., Clark, K.J., Biasi, G.P., Langridge, R.M., Villamor, P., 2012. Major earthquakes occur regularly on an isolated plate boundary fault. Science 336, 1690–1693.
Bickle, M.J., McKenzie, D., 1987. The transport of heat and matter by fluids during metamorphism. Contrib. Mineral. Petrol. 95, 384–392.
Blanpied, M.L., Lockner, D.A., Byerlee, J.D., 1992. An earthquake mechanism based on rapid sealing of faults. Nature 358, 574–576.
Boese, C.M., Townend, J., Smith, E., Stern, T., 2012. Microseismicity and stress in the vicinity of the Alpine Fault, central Southern Alps, New Zealand. J. Geophys. Res., Solid Earth 117, B02302.
Boulton, C., Carpenter, B.M., Toy, V., Marone, C., 2012. Physical properties of surface outcrop cataclastic fault rocks, Alpine Fault, New Zealand. Geochem. Geophys. Geosyst. 13, Q01018.
Byerlee, J., 1993. Model for episodic flow of high-pressure water in fault zones before earthquakes. Geology 21, 303–306.
Carpenter, B.M., Kitajima, H., Sutherland, R., Townend, J., Toy, V.G., Saffer, D.M., 2014. Hydraulic and acoustic properties of the active Alpine Fault, New Zealand: laboratory measurements on DFDP-1 drill core. Earth Planet. Sci. Lett. 390, 45–51.
Cox, S.C., Menzies, C.D., Sutherland, R., Denys, P.H., Chamberlain, C., Teagle, D.A.H., 2015. Changes in hot spring temperature and hydrogeology of the Alpine Fault hanging wall, New Zealand, induced by distal South Island earthquakes. Geofluids 15, 216–239.
Cox, S.C., Sutherland, R., 2007. Regional geological framework of South Island, New Zealand, and its significance for understanding the active plate boundary. In: Okaya, D., Stern, T., Davey, F. (Eds.), A Continental Plate Boundary: Tectonics at South Island, New Zealand. American Geophysical Union, Washington DC, pp. 19–46.
Craw, D., Norris, R.J., 1993. Grain boundary migration of water and carbon dioxide during uplift of garnet-zone Alpine Schist, New Zealand. J. Metamorph. Geol. 11, 371–378.
de Leeuw, G.A.M., Hilton, D.R., Güleç, N., Mutlu, H., 2010. Regional and temporal variations in $CO_2/^3He$, $^3He/^4He$ and $\delta^{13}C$ along the North Anatolian Fault Zone, Turkey. Appl. Geochem. 25, 524–539.
Faulkner, D.R., Rutter, E.H., 2001. Can the maintenance of overpressured fluids in large strike-slip fault zones explain their apparent weakness? Geology 29, 503–506.
Fulton, P.M., Saffer, D.M., 2009. Potential role of mantle-derived fluids in weakening the San Andreas Fault. J. Geophys. Res., Solid Earth 114, B07408.
Fulton, P.M., Saffer, D.M., Bekins, B.A., 2009. A critical evaluation of crustal dehydration as the cause of an overpressured and weak San Andreas Fault. Earth Planet. Sci. Lett. 284, 447–454.
Giggenbach, W.F., Sano, Y., Wakita, H., 1993. Isotopic composition of helium, and CO_2 and CH_4 contents in gases produced along the New Zealand part of a convergent plate boundary. Geochim. Cosmochim. Acta 57, 3427–3455.

Harris, M., Coggon, R.M., Smith-Duque, C.E., Cooper, M.J., Milton, J.A., Teagle, D.A.H., 2015. Channelling of hydrothermal fluids during the accretion and evolution of the upper oceanic crust: Sr isotope evidence from ODP Hole 1256D. Earth Planet. Sci. Lett. 416, 56–66.

Hilton, D.R., Porcelli, D., 2003. Noble gases as mantle tracers. In: Turekian, H.D., Holland, K.K. (Eds.), Treatise on Geochemistry. Pergamon, Oxford, pp. 277–318.

Horton, T.W., Blum, J.D., Craw, D., Koons, P.O., Chamberlain, C.P., 2003. Oxygen, carbon, and strontium isotopic constraints on timing and sources of crustal fluids in an active orogen: South Island, New Zealand. N.Z. J. Geol. Geophys. 46, 457–471.

Jenkin, G.R.T., Craw, D., Fallick, A.E., 1994. Stable isotopic and fluid inclusion evidence for meteoric fluid penetration into an active mountain belt: Alpine Schist, New Zealand. J. Metamorph. Geol. 12, 429–444.

Jiracek, G.R., Gonzalez, V.M., Caldwell, T.G., Wannamaker, P.E., Kilb, D., 2007. Seismogenic, electrically conductive, and fluid zones at continental plate boundaries in New Zealand, Himalaya, and California, USA. In: Okaya, D., Stern, T., Davey, F. (Eds.), A Continental Plate Boundary: Tectonics at South Island, New Zealand. American Geophysical Union, Washington, DC, pp. 347–369.

Kennedy, B.M., Kharaka, Y.K., Evans, W.C., Ellwood, A., DePaolo, D.J., Thordsen, J., Ambats, G., Mariner, R.H., 1997. Mantle fluids in the San Andreas Fault system, California. Science 278, 1278–1281.

Klemperer, S.L., Kennedy, B.M., Sastry, S.R., Makovsky, Y., Harinarayana, T., Leech, M.L., 2013. Mantle fluids in the Karakoram fault: helium isotope evidence. Earth Planet. Sci. Lett. 366, 59–70.

Koons, P.O., 1987. Some thermal and mechanical consequences of rapid uplift: an example from the Southern Alps, New Zealand. Earth Planet. Sci. Lett. 89, 307–319.

Koons, P.O., 1990. Two-sided orogen: collision and erosion from the sandbox to the Southern Alps, New Zealand. Geology 18, 679–682.

Kulongoski, J.T., Hilton, D.R., Barry, P.H., Esser, B.K., Hillegonds, D., Belitz, K., 2013. Volatile fluxes through the Big Bend section of the San Andreas Fault, California: helium and carbon-dioxide systematics. Chem. Geol. 339, 92–102.

Lamb, S., Smith, E., Stern, T., Warren-Smith, E., 2015. Continent-scale strike-slip on a low-angle fault beneath New Zealand's Southern Alps: implications for crustal thickening in oblique collision zones. Geochem. Geophys. Geosyst. 16, 3076–3096.

Lockner, D., Tanaka, H., Ito, H., Ikeda, R., Omura, K., Naka, H., 2009. Geometry of the Nojima Fault at Nojima-Hirabayashi, Japan – I. A simple damage structure inferred from borehole core permeability. Pure Appl. Geophys. 166, 1649–1667.

Manning, C.E., Ingebritsen, S.E., 1999. Permeability of the continental crust: implications of geothermal data and metamorphic systems. Rev. Geophys. 37, 127–150.

Marty, B., Jambon, A., 1987. $C/^3He$ in volatile fluxes from the solid Earth: implications for carbon geodynamics. Earth Planet. Sci. Lett. 83, 16–26.

Menzies, C.D., Teagle, D.A.H., Craw, D., Cox, S.C., Boyce, A.J., Barrie, C.D., Roberts, S., 2014. Incursion of meteoric waters into the ductile regime in an active orogen. Earth Planet. Sci. Lett. 399, 1–13.

Niedermann, S., Bach, W., Erzinger, J., 1997. Noble gas evidence for a lower mantle component in MORBs from the southern East Pacific rise: decoupling of helium and neon isotope systematics. Geochim. Cosmochim. Acta 61, 2697–2715.

Norris, R.J., Cooper, A.F., 2007. The Alpine Fault, New Zealand: surface geology and field relations. In: Okaya, D., Stern, T., Davey, F. (Eds.), A Continental Plate Boundary: Tectonics at South Island, New Zealand. American Geophysical Union, Washington, DC, pp. 157–175.

O'Neil, J., 1984. Water–rock interactions in fault gouge. Pure Appl. Geophys. 122, 440–446.

Pickett, D.A., Wasserburg, G.J., 1989. Neodymium and strontium isotopic characteristics of New Zealand granitoids and related rocks. Contrib. Mineral. Petrol. 103, 131–142.

Pitcairn, I.K., Craw, D., Teagle, D.A.H., 2014. The gold conveyor belt: large-scale gold mobility in an active orogen. Ore Geol. Rev. 62, 129–142.

Rice, J.R., 1992. Fault stress states, pore pressure distributions, and the weakness of the San Andreas Fault. In: Brian, E., Teng-fong, W. (Eds.), International Geophysics. Academic Press, pp. 475–503. Chapter 20.

Schleicher, A.M., Sutherland, R., Townend, J., Toy, V.G., van der Pluijm, B.A., 2015. Clay mineral formation and fabric development in the DFDP-1B borehole, central Alpine Fault, New Zealand. N.Z. J. Geol. Geophys. 58, 13–21.

Sibson, R.H., 1992. Implications of fault-valve behaviour for rupture nucleation and recurrence. Tectonophysics 211, 283–293.

Sims, A., Cox, S.C., Fitzsimons, S.J., Holland, P., 2015. Seasonal infiltration and groundwater movement in schist bedrock, Southern Alps, New Zealand. J. Hydrol., N.Z. 54, 33–52.

Sleep, N.H., Blanpied, M.L., 1992. Creep, compaction and the weak rheology of major faults. Nature 359, 687–692.

Sutherland, R., Eberhart-Phillips, D., Harris, R.A., Stern, T., Beavan, J., Ellis, S., Henrys, S., Cox, S., Norris, R.J., Berryman, J.R., Townend, J., Bannister, S., Pettinga, J., Leitner, B., Little, T., Cooper, A.F., Yetton, M., Stirling, M., 2007. Do great earthquakes occur on the Alpine Fault in central South Island, New Zealand? In: Okaya, D., Stern, T., Davey, F. (Eds.), A Continental Plate Boundary: Tectonics at South Island, New Zealand. American Geophysical Union, Washington, DC, pp. 235–251.

Sutherland, R., Toy, V.G., Townend, J., Cox, S.C., Eccles, J.D., Faulkner, D.R., Prior, D.J., Norris, R.J., Mariani, E., Boulton, C., Carpenter, B.M., Menzies, C.D., Little, T.A., Hasting, M., De Pascale, G.P., Langridge, R.M., Scott, H.R., Reid-Lindroos, Z., Fleming, B., Kopf, A.J., 2012. Drilling reveals fluid control on architecture and rupture of the Alpine Fault, New Zealand. Geology 40, 1143–1146.

Toy, V.G., Boulton, C.J., Sutherland, R., Townend, J., Norris, R.J., Little, T.A., Prior, D.J., Mariani, E., Faulkner, D., Menzies, C.D., Scott, H., Carpenter, B.M., 2015. Fault rock lithologies and architecture of the central Alpine fault, New Zealand, revealed by DFDP-1 drilling. Lithosphere 7, 206.

Tulloch, A.J., Ramezani, J., Kimbrough, D.L., Faure, K., Allibone, A.H., 2009. U–Pb geochronology of mid-Paleozoic plutonism in western New Zealand: implications for S-type granite generation and growth of the east Gondwana margin. Geol. Soc. Am. Bull. 121, 1236–1261.

Van Avendonk, H.J.A., Holbrook, W.S., Okaya, D., Austin, J.K., Davey, F., Stern, T., 2004. Continental crust under compression: a seismic refraction study of South Island geophysical transect I, South Island, New Zealand. J. Geophys. Res. 109, B06302.

Wannamaker, P.E., Jiracek, G.R., Stodt, J.A., Caldwell, T.G., Gonzalez, V.M., McKnight, J.D., Porter, A.D., 2002. Fluid generation and pathways beneath an active compressional orogen, the New Zealand Southern Alps, inferred from magnetotelluric data. J. Geophys. Res. 107. ETG 6-1–ETG 6-20.

Warr, L.N., Cox, S.C., 2001. Clay mineral transformations and weakening mechanisms along the Alpine Fault, New Zealand. Geol. Soc. (Lond.) Spec. Publ. 186, 85–101.